Frustrated Kondo chains and glassy magnetic phases on the pyrochlore lattice

Jing Luo and Gia-Wei Chern
Department of Physics, University of Virginia, Charlottesville, Virginia 22904, USA

(Received 6 April 2018; revised manuscript received 9 October 2018; published 13 December 2018)

We present an extensive numerical study of a type of frustrated itinerant magnetism on the pyrochlore lattice. In this theory, the pyrochlore magnet can be viewed as a cross-linking network of Kondo or double-exchange chains. Contrary to models based on Mott insulators, this itinerant magnetism approach provides a natural explanation for several spin and orbital superstructures observed on the pyrochlore lattice. Through extensive Monte Carlo simulations, we obtain the phase diagrams at two representative electron filling fractions $n = \frac{1}{2}$ and $\frac{2}{3}$. In particular, we show that an intriguing glassy magnetic state characterized by ordering wave vectors $\mathbf{q} = (\frac{1}{3}, \frac{1}{3}, 1)$ gives a rather satisfactory description of the low-temperature phase recently observed in spinel $GeFe_2O_4$.

DOI: 10.1103/PhysRevB.98.214423

I. INTRODUCTION

Highly frustrated magnets continue to fascinate physicists with intriguing and sometimes unexpected magnetic phases. This is particularly true for spin systems exhibiting strong geometrical frustration such as pyrochlore antiferromagnets [1]. Conventionally, frustrated magnets are modeled by the Heisenberg Hamiltonian $\mathcal{H} = \sum_{ij} J_{ij}\mathbf{S}_i \cdot \mathbf{S}_j$ within the framework of Mott insulators. For pyrochlore and kagome lattices, the frustrated nearest-neighbor antiferromagnetic spin interactions give rise to a macroscopic ground-state degeneracy [2,3]. This in turn makes the magnets highly susceptible to small perturbations. Removal of the extensive degeneracy by perturbations beyond J_1 leads to unusual spin ordering and even unconventional magnetic phases [4,5]. For systems with degenerate orbitals, a good starting point is the Kugel-Khomskii Hamiltonian [6], which has been successfully employed to understand spin-orbital ordering in frustrated magnets [7–9].

Recently, complex spin and/or orbital superstructures observed in spinels such as $CuIr_2S_4$ [10,11], $MgTi_2O_4$ [12], and ZnV_2O_4 [13] have posed an intriguing theoretical challenge. Several models have been proposed to explain the experimental results. However, understanding these unusual orderings within the framework of Mott insulators often requires fine tuning or sometimes *ad hoc* perturbations. On the other hand, it has been demonstrated in many cases that approaches based on itinerant magnetism provide a very natural explanation for the observed superstructures [14–16]. For example, the octamer order in $CuIr_2S_4$ and chiral distortion in $MgTi_2O_4$ can be explained as resulting from an orbital-driven Peierls instability [14,17]. Moreover, several of these compounds have been shown to be a bad insulator, indicating that these magnets are in the vicinity of metal-insulator transition [18–21]. Recent experiments further support the picture of orbital-Peierls state [22,23].

The itinerant approach also naturally explains the $\mathbf{q} = (0, 0, 1)$ magnetic structure of ZnV_2O_4, which consists of $\uparrow\uparrow\downarrow\downarrow\ldots$ spin chains along [110] directions of the pyrochlore lattice [15,16]. Essentially, taking into account the reduced dimensionality of electron hopping in such systems, this interesting commensurate one-dimensional (1D) order can be understood as resulting from the spin-induced nesting instability of 1D Kondo chains. Another interesting example is the multiple-$\mathbf{q}$ magnetic ordering recently observed in spinel $GeFe_2O_4$ [24]. At low temperatures, neutron-scattering experiments found diffusive peaks centered at $\mathbf{q} = (\frac{1}{3}, \frac{1}{3}, 1)$ and other symmetry-related wave vectors, implying a quasi-1D ordering with a tripled unit cell. Stabilization of this unusual commensurate magnetic order seems rather difficult using the localized spin models.

In this paper, we present a detailed numerical study of a frustrated itinerant spin model for spinel compounds AB_2X_4. In these materials, the octahedral crystal field splits the $3d$ orbitals of the B-site magnetic ion into a t_{2g} triplet and a higher-energy e_g doublet. Keeping only the dominant $dd\sigma$ transfer integral between the low-energy t_{2g} orbitals, electron hoppings on the pyrochlore lattice can be modeled by a set of one-dimensional (1D) tight-binding chains in this leading-order approximation [15]. Inclusion of the onsite Hubbard and Hund's interactions within the mean-field approximation then leads to Kondo or double-exchange type electron-spin couplings. A minimum model is given by a collection of cross-linking Kondo chains running along the $\langle 110\rangle$ directions of the pyrochlore lattice. Importantly, commensurate 1D spin order can arise naturally as a result of Fermi-point nesting instability in Kondo chains with a rational electron filling fraction. A different type of geometrical frustration then results from the fact that the favored 1D spin order cannot be realized on all chains simultaneously, leading to three-dimensional (3D) magnetic order and to glassy behavior in some cases.

II. MODEL AND METHOD

Our itinerant electron approach to magnetic orders in spinels is based on a mean-field treatment of Hubbard-type Hamiltonian. First, we consider the tight-binding model of t_{2g} orbitals in spinels. As discussed above, the magnetic ions in

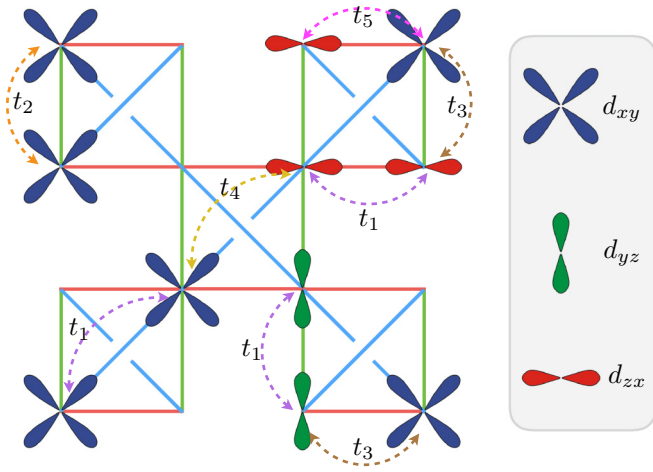

FIG. 1. The inequivalent transfer integrals between the three t_{2g} orbitals on the pyrochlore lattice: $t_1 = \frac{3}{4}V_{dd\sigma} + \frac{1}{4}V_{dd\delta}$, $t_2 = \frac{1}{2}V_{dd\pi} + \frac{1}{2}V_{dd\delta}$, $t_3 = \frac{1}{2}V_{dd\pi} - \frac{1}{2}V_{dd\delta}$, $t_4 = t_5 = 0$.

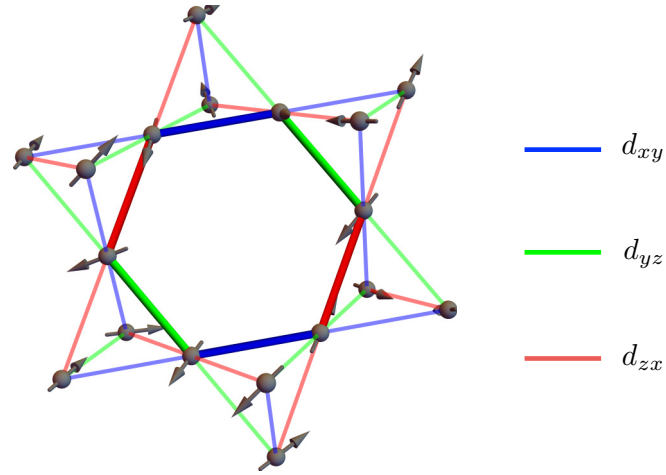

FIG. 2. Schematic diagram showing the shortest hexagonal loops in the pyrochlore lattice. The three different colors indicate distinct Kondo chains occupied by the three t_{2g} orbitals.

spinels form a pyrochlore lattice. Figure 1 shows some representative hopping processes of t_{2g} electrons on the pyrochlore lattice. Here, the various hopping integrals are computed using the Slater-Koster formula; the results can be expressed in terms of fundamental bond integrals $V_{dd\sigma}$, $V_{dd\pi}$, and $V_{dd\delta}$ [25]. In general, the σ bond integral is much stronger than the π and δ bonds. To the leading-order approximation, we thus neglect contributions from $V_{dd\pi}$ and $V_{dd\delta}$ to the various bond integrals. As a result, only the t_1 hopping remains in this approximation, which means only those nearest-neighbor hoppings between the same type of orbitals among appropriate chains dominate, namely, d_{xy} along $\langle 110\rangle$, $\langle 1\bar{1}0\rangle$, d_{yz} along $\langle 011\rangle$, $\langle 01\bar{1}\rangle$ and d_{zx} along $\langle 101\rangle$, $\langle \bar{1}01\rangle$ (see Fig. 1).

Next, we consider the onsite interactions which are dictated by the multiorbital Hubbard-Kanamori interaction $\mathcal{H}_U$ [26]. Since we are interested in solutions with nonzero local moment, we use the Hartree-Fock mean-field method to decouple the interaction terms. The mean-field decoupling gives rise to a Kondo-type electron-spin coupling $\mathcal{H}_U = U_{\rm eff}\langle\hat{\mathbf{s}}_i\rangle\cdot\hat{\mathbf{s}}_i$, where $\mathbf{s}_i$ is the electron spin operator, and $U_{\rm eff}$ is an effective Hubbard parameter. For example, for t_{2g} orbitals, $U_{\rm eff} = 4(U/9 + 4J_H/9)$, where U and J_H are the onsite Hubbard repulsion and Hund's coupling, respectively. In the case of $GeFe_2O_4$, the magnetic Fe^{2+} ions have a $t_{2g}^4\, e_g^2$ electron configuration. Due to strong intraorbital Hubbard interaction and Hund's coupling, the two e_g electrons remain in the correlated $S = 1$ state. The remaining t_{2g}^4 electrons thus form conduction band with a filling fraction $n = \frac{2}{3}$.

We thus arrive at the following Hamiltonian describing cross-linking Kondo chains on the pyrochlore lattice in Fig. 2:

$$\mathcal{H} = -t\sum_{\mu,\sigma}\sum_{\langle ij\rangle\|\mu}(\hat{c}^\dagger_{i\,\mu\sigma}\,\hat{c}_{j\mu\sigma} + \text{H.c.}) - J\sum_{i,\mu}\mathbf{S}_i\cdot\hat{\mathbf{s}}_{i,\mu}, \quad (1)$$

where $\hat{c}^\dagger_{i,\mu\sigma}$ is the creation operator for electron with spin $\sigma = \uparrow, \downarrow$ and orbital flavor $\mu = xy$, yz, zx at site i, $\langle ij\rangle \| \mu$ indicates the nearest-neighbor (NN) pair along the $\langle 110\rangle$ direction that corresponds to the active t_{2g} orbital μ, the hopping constant t is set to be 1 in all the simulations below, $J \approx U_{\rm eff}\langle\hat{\mathbf{s}}\rangle$ is the effective Hund's coupling, $\mathbf{S}_i$ is the $O(3)$ local magnetic moment, and $\hat{\mathbf{s}}_{i,\mu} = \sum_{\alpha,\beta} c^\dagger_{i\mu\alpha}\boldsymbol{\sigma}_{\alpha\beta}c_{i\mu\beta}$ is the electron spin operator.

The 1D ferromagnetic Kondo chain, which is the backbone of Hamiltonian (1), has been extensively studied over the years [27–29]. However, the fact that every local spin $\mathbf{S}_i$ is shared by three Kondo chains introduces competition between different chains. In particular, the cross-linking Kondo chains exhibit a type of geometrical frustration since the electronic energy of neighboring chains cannot be simultaneously minimized. For example, the shortest hexagonal loops (Fig. 2) of spins on the pyrochlore lattice contain sites which belong to six different Kondo chains. Consequently, the nearest-neighbor spin-spin correlation favored by individual chains might not be able to extend over the hexagonal loop consistently, leading to frustrated interactions.

Since our main interest is in the potential magnetic orderings of this model, we will assume classical local spins here. However, even with classical local spins, Monte Carlo simulations of Kondo-lattice models are a challenging task mainly due to the nonlocal electron-mediated effective interactions between the local moments. Indeed, in the weak-coupling limit $J \ll t$, integrating out the electrons gives rise to a long-range Ruderman-Kittel-Kasuya-Yosida (RKKY) type spin interactions. For large J, one needs to diagonalize the electron tight-binding Hamiltonian that depends on the spin configuration for each Monte Carlo update. For a pyrochlore lattice of linear size L, there are $N = 16L^3$ spins and the dimension of a generic spinful and orbitally degenerate tight-binding (TB) Hamiltonian is $D = 2\times 3\times N = 96L^3$. This severely limits the largest accessible lattice sizes, as exact diagonalization scales as $\mathcal{O}(D^3)$ and is computationally very costly. However, thanks to the 1D nature of the TB model in Eq. (1), each local spin update only requires diagonalizing three chains whose dimension is $D_{\rm 1D} = 4L$. Specifically, we adopt the standard local Metropolis Monte Carlo method. For a randomly chosen spin, say at site i, we consider rotating the spin from $\mathbf{S}_i$ to $\mathbf{S}'_i$. The energy cost associated with this update comes from the electron energy of the three Kondo chains intersecting at this

site, i.e.,

$$\Delta E = \sum_{\mu=xy,yz,zx} \left[\sum_{m=1}^{N_f} \left(\varepsilon_m^{(\mu)}(\mathbf{S}_i') - \varepsilon_m^{(\mu)}(\mathbf{S}_i) \right) \right]. \quad (2)$$

Here, $\varepsilon_m^{(\mu)}$ are the eigenenergies of the μ-orbital Kondo chain and N_f is the number of occupied electrons determined by the filling fraction. Once ΔE is obtained by exactly diagonalizing the three chains intersecting at $\mathbf{S}_i$, the spin update is accepted according to the standard Metropolis algorithm with a probability $p_{\rm acc} = \min[1, \exp(-\Delta E/k_B T)]$. The computational cost of each update thus scales as $\mathcal{O}(D_{\rm 1D}^3) \sim \mathcal{O}(N)$. Each sweep is completed by updating local spins sequentially. The Monte Carlo simulation for the coupled chains is still costly with an overall scaling $\mathcal{O}(N \times D_{\rm 1D}^3) \sim \mathcal{O}(N^2)$, but the efficiency is much improved compared with the full 3D tight-binding model.

III. PHASE DIAGRAM

In this section we obtain the phase diagram of Hamiltonian (1) for two representative filling fractions $n = \frac{1}{2}$ and $\frac{2}{3}$ based on extensive Monte Carlo simulations; the results are summarized in Fig. 3.

We first discuss the simpler case of half-filling. There is only one ordered phase characterized by the noncoplanar all-in–all-out (AIAO) spin order at low temperatures; see Fig. 3(a). For a half-filled Kondo chain, the nesting of the Fermi points favors a collinear Néel order with doubled unit cell, i.e., $\uparrow\downarrow\uparrow\downarrow\ldots$. However, it is easy to convince oneself that such collinear ordering cannot be simultaneously realized in the three different chains on the pyrochlore lattice; a manifestation of the geometrical frustration is discussed above. The solution to this conflicted situation is the AIAO order in which a 1D spin order with a doubled unit cell, albeit with noncollinear spins, still gaps out the Fermi points and lowers the overall energy. The AIAO order is characterized by three nonzero staggered magnetizations: $\mathbf{L}_1 = \mathbf{S}_0 + \mathbf{S}_1 - \mathbf{S}_2 - \mathbf{S}_3$,

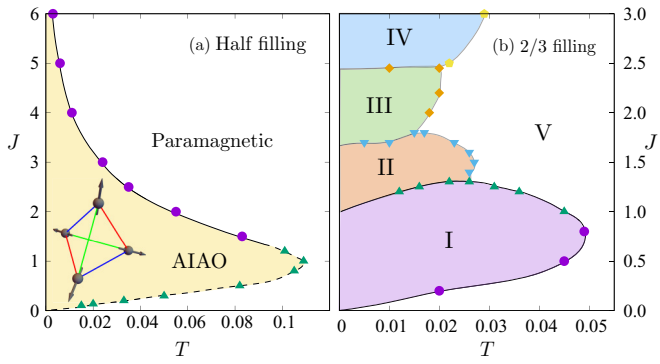

FIG. 3. The phase diagrams for (a) half-filling and (b) $\frac{2}{3}$ filling. Solid and dashed lines represent first- and second-order phase transitions, respectively, in both (a) and (b). For half-filling, two phases are all-in–all-out phase (AIAO), paramagnetic phase. For $\frac{2}{3}$ filling, phases are (I) $\mathbf{q} = (\frac{1}{3}, \frac{1}{3}, 1)$ order, (II) $(\frac{1}{2}, \frac{1}{2}, \frac{1}{2})$ order, (III) a unknown magnetic phase characterized by a large spin nematic order parameter, (IV) ferromagnetic phase, and (V) paramagnetic phase.

and the symmetry related $\mathbf{L}_2$ and $\mathbf{L}_3$. Here, $\mathbf{S}_m$ denotes the spin of the mth sublattice (there are four sublattices) of the pyrochlore lattice. A perfect AIAO has $|\mathbf{L}_1| = |\mathbf{L}_2| = |\mathbf{L}_3|$ while their orientations satisfy $\mathbf{L}_1 \perp \mathbf{L}_2 \perp \mathbf{L}_3$. Due to the noncoplanar nature of this magnetic order, the AIAO phase further breaks a Z_2 chiral symmetry which is measured by the discrete scalar spin chirality $\chi = \mathbf{L}_1 \cdot (\mathbf{L}_2 \times \mathbf{L}_3)$. The phase boundary of the AIAO order, shown in Fig. 3(a), is determined from the Binder crossing of corresponding staggered order parameters for continuous phase transition at small J.

Interestingly, the transition becomes first order at large J. As in general Kondo-lattice or double-exchange models, the effective Hamiltonian in the large-J limit is given by a Heisenberg model with a dominant NN exchange $J_{\rm AF} \sim t^2/J$. This can be understood as follows. In the $J \to \infty$ limit at half-filling, electrons are localized in individual orbitals of each site with their spins aligned with the local moments. This gives rise to a huge degeneracy which is lifted by the electron hopping. Due to Pauli exclusion principle, electrons can hop to neighboring sites only when their spins are not aligned, thus favoring an antiferromagnetic interaction. Specifically, the effective Hamiltonian corresponds to the energy gain through the second-order process, which is $E_{ij}^{(2)} \approx -[t\,\langle\chi_i|\chi_j\rangle]^2/J$, where $|\chi_i\rangle$ is the local electron spinor wave function. Since Pauli exclusion requires that the spins at i and j must be antialigned in order to allow the electrons hop to the NN sites, the inner product of the spinor eigenstates $\langle\chi_i|\chi_j\rangle = \sin(\theta_{ij}/2)$, where θ_{ij} is the angle between the two local spins. Consequently, we obtain an effective spin interaction: $E_{ij}^{(2)} = J_{\rm AF}\,\mathbf{S}_i \cdot \mathbf{S}_j$ up to a constant, with $J_{\rm AF} \sim t^2/J$.

It is interesting to note that the frustrated nature of the coupled Kondo chains in the large-J limit corresponds to the well-known geometrical frustration of AF Heisenberg model on the pyrochlore lattice. The huge ground-state degeneracy of this model leads to a low-temperature spin liquid phase. Contrary to the high-temperature paramagnetic phase, disordered spins in this classical spin liquid exhibit strong short-range correlation [3]. A possible scenario is that the system first enters a correlated classical spin-liquid regime at $T \sim J_{\rm AF}$, then undergoes a phase transition at a lower T_c into the AIAO phase. Our detailed analysis shows that the classical spin-liquid phase is preempted by the first-order transition, and the system immediately goes to the AIAO phase at a critical $T_c \sim J_{\rm AF}$.

We now turn to the case of $\frac{2}{3}$ filling. Before discussing the phase diagram of coupled Kondo chains on the pyrochlore lattice, we first consider the ground states of a single Kondo chain. The Fermi wave vector of a $\frac{2}{3}$-filled 1D band is $k_F = 2\pi/3\ell$, where $\ell = \sqrt{2}a/4$ is the 1D lattice constant and a is the size of the cubic unit cell. The system is thus susceptible to perturbations with a wave vector $q = 2k_F = 4\pi/3\ell$ that gaps out the two Fermi points; see Fig. 4. Indeed, our Monte Carlo simulations on a single Kondo chain find a magnetic order with a tripled unit cell at $T \to 0$ and small J. The three spins within the extended unit cell are coplanar, with a relative angle very close to 120°; more details can be found in the Appendix.

Next, we apply the above 1D results to understand the ground states of coupled Kondo chains in 3D, which is particularly important in explaining the magnetic order of

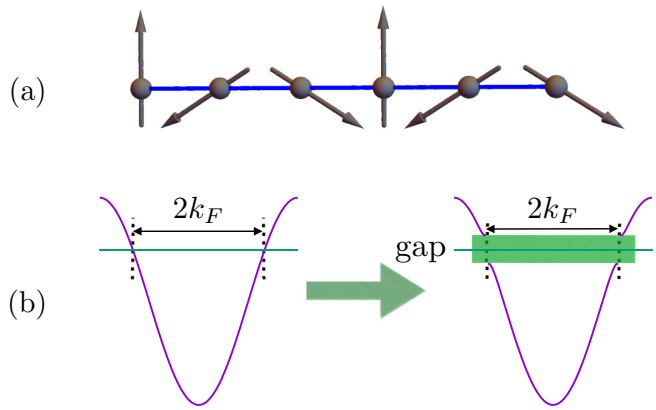

FIG. 4. (a) The $T \to 0$ ground state of a single Kondo chain. The long-range spin order is characterized by a tripled unit cell with a coplanar almost 120° structure within a unit cell. (b) Shows the gap opening of a ($n = \frac{2}{3}$)-filled Kondo chain due to Fermi-point nesting.

spinel $GeFe_2O_4$ where the t_{2g} orbitals are $\frac{2}{3}$ filled. From direct inspection of the geometry, one immediately realizes that the above coplanar 1D ground state cannot be consistently combined in the 3D pyrochlore lattice. This is another manifestation of the geometrical frustration discussed in Fig. 2. Contrary to the half-filling case, where the frustrated coupling leads to the AIAO long-range order, there is no simple magnetic structure selected in the $\frac{2}{3}$-filling case. A snapshot of spin configuration from our Monte Carlo simulations is shown in Fig. 5(a). Individual Kondo chains are clearly not in their 1D ground state discussed above. In fact, spins on a given chain are not even coplanar. Although no clear pattern can be seen from this snapshot, detailed characterization shows that a long-range spin-spin correlation with a tripled unit cell nonetheless is developed along each individual chain of the 3D lattice; see Fig. 6(a). Moreover, the 3D noncoplanar spin order is characterized by multiple wave vectors that are related to $\mathbf{q} = (\frac{1}{3}, \frac{1}{3}, 1)$ by symmetry, as shown in the inset of Fig. 6(a).

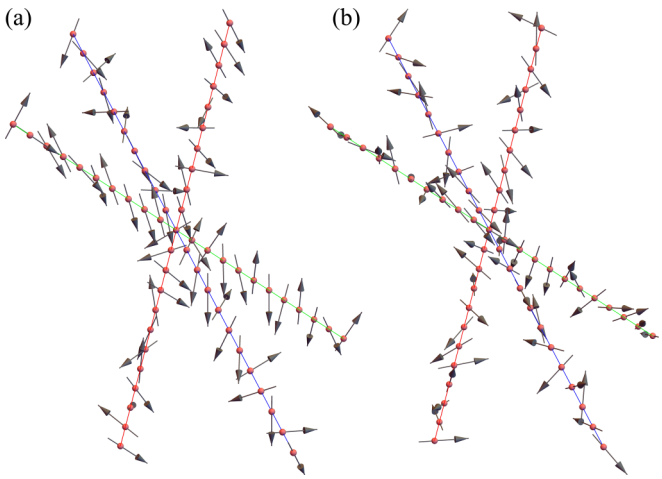

FIG. 5. Snapshots of the local spin configurations for (a) the $\mathbf{q} = (\frac{1}{3}, \frac{1}{3}, 1)$ order and (b) $\mathbf{q} = (\frac{1}{2}, \frac{1}{2}, \frac{1}{2})$ order.

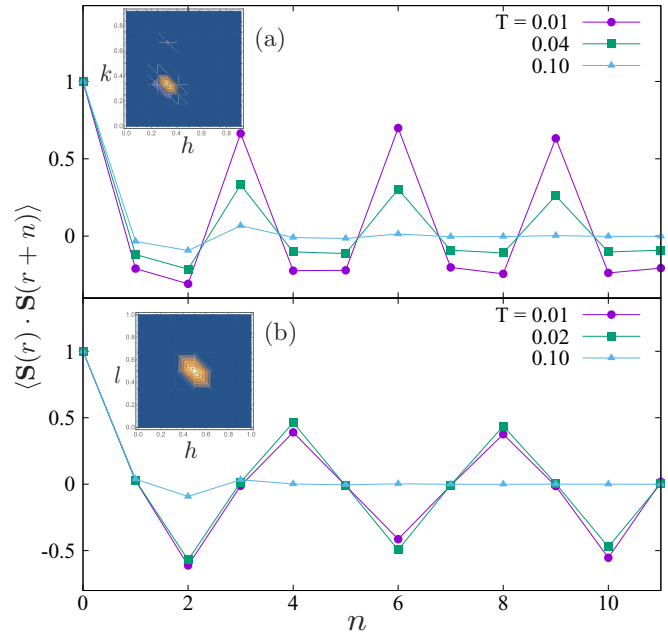

FIG. 6. The spin-spin correlation function $\langle \mathbf{S}(r) \cdot \mathbf{S}(r+n) \rangle$ averaged over all Kondo chains of the pyrochlore lattice for (a) the $\mathbf{q} = (\frac{1}{3}, \frac{1}{3}, 1)$ and (b) the $\mathbf{q} = (\frac{1}{2}, \frac{1}{2}, \frac{1}{2})$ order at $n = \frac{2}{3}$ filling with (a) $J = 1$ for and (b) $J = 1.5$. The insets show the corresponding structure factor on the (a) $\mathbf{q} = (h, k, 1)$ and (b) $\mathbf{q} = (h, h, l)$ planes.

From the phase diagram of single Kondo chain discussed in the Appendix, the magnetic order at large J cannot be understood from the Fermi-point nesting picture. Here, we performed extensive Monte Carlo simulations to obtain the ($n = \frac{2}{3}$)-filling phase diagram, shown in Fig. 3(b). At small Hund's coupling, the low-T phase is a magnetic order characterized by multiple ordering wave vectors that are related to $\mathbf{q} = (\frac{1}{3}, \frac{1}{3}, 1)$, as discussed above. Several unusual magnetic structures are obtained at larger J. The phase boundaries are mostly first order, except for the small-J regime (purple dots) where the phase transition between paramagnetic and $(\frac{1}{3}, \frac{1}{3}, 1)$-ordered phases might be continuous.

The various 3D phases are loosely related to their 1D counterpart. Upon increasing J, the ordering wave vectors first change from $\mathbf{q} = (\frac{1}{3}, \frac{1}{3}, 1)$ to $(\frac{1}{2}, \frac{1}{2}, \frac{1}{2})$ at $J \approx t$. The system undergoes another first-order transition at $J \approx 1.6t$ into an unknown magnetic order (phase III) that is characterized by rather large nematic order parameter. We have checked that spins are pretty much frozen in this phase, yet no clear long-range order can be seen from the static structure factor. And, finally, the ferromagnetic order takes over as the ground state when $J \gtrsim 2.5t$. An interesting case is the $\mathbf{q} = (\frac{1}{2}, \frac{1}{2}, \frac{1}{2})$ phase at intermediate Hund's coupling $1 \lesssim J \lesssim 1.6$ (phase II in the phase diagram). A snapshot of local spin configurations on three different chains intersecting at one spin is shown in Fig. 5(b). Again, although no clear ordering pattern can be found in the snapshot, detailed analysis showed that individual Kondo chains exhibit a clear 1D spin correlation with a quadrupled unit cell, as shown in Fig. 6(b). This is in stark contrast to the ground state of a single Kondo chain in the same J regime, where the $T \to 0$ ground state is a multiple-q noncoplanar order. In this case, the "frustrated" interchain

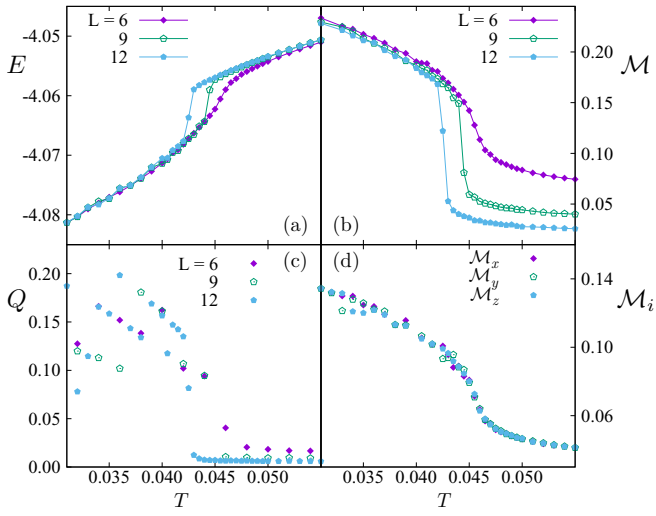

FIG. 7. The temperature dependence of some quantities for the $\frac{2}{3}$-filled coupled Kondo chains with $J = 1$. (a) The energy density and (b) the magnetic order parameter $\mathcal{M}$ show the first-order phase transition. (c) The nematic order parameter Q bifurcates into multiple branches below the phase transition point. (d) The partial magnetic order parameters, $\mathcal{M}_x, \mathcal{M}_y, \mathcal{M}_z$, which are summation of $\mathbf{\Phi}_m$ at wave vectors $\mathbf{q}_m = (1, \pm\frac{1}{3}, \pm\frac{1}{3})$, $(\pm\frac{1}{3}, 1, \pm\frac{1}{3})$, $(\pm\frac{1}{3}, \pm\frac{1}{3}, 1)$, respectively, with $L = 6$ show no significant difference at low temperatures.

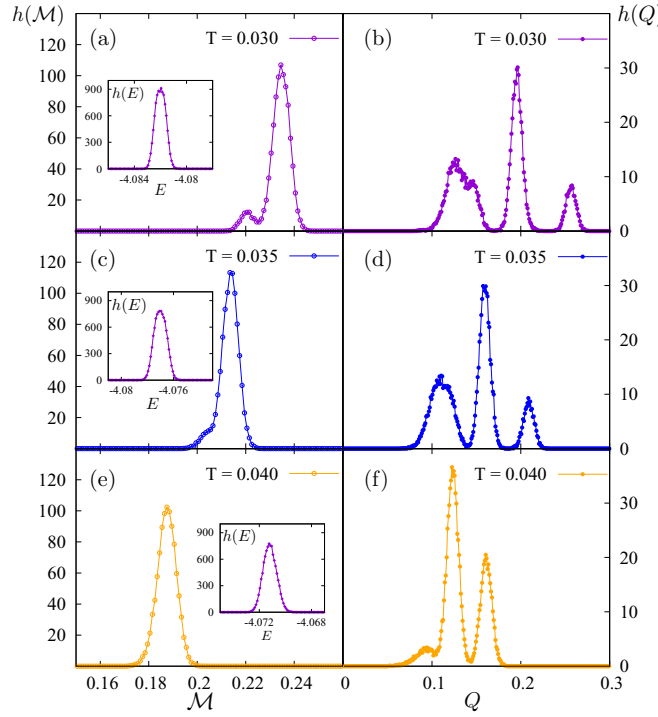

FIG. 8. Probability distribution function for the magnetic order parameter $\mathcal{M}$, the nematic order parameter Q, and the energy density E (insets) at three different temperatures below T_c. These curves are obtained from extensive Monte Carlo simulations on lattices of $J = 1$, $L = 9$.

coupling actually stabilizes the quadrupled chains and the $\mathbf{q} = (\frac{1}{2}, \frac{1}{2}, \frac{1}{2})$ order on the pyrochlore lattice.

IV. QUASIDEGENERACY AND GLASSY BEHAVIORS OF THE $\mathbf{q} = (\frac{1}{3}, \frac{1}{3}, 1)$ PHASE

To characterize the complex multiple-$\mathbf{q}$ magnetic order in the $\mathbf{q} = (\frac{1}{3}, \frac{1}{3}, 1)$ phase, we introduce vector order parameters $\mathbf{\Phi}_m \equiv (1/N) \sum_j \mathbf{S}_j \exp(i\mathbf{q}_m \cdot \mathbf{r}_j)$, which are the Fourier modes of spins at the 12 symmetry-related wave vectors $\mathbf{q}_m = (\pm\frac{1}{3}, \pm\frac{1}{3}, 1)$, $(\pm\frac{1}{3}, 1, \pm\frac{1}{3})$, and $(1, \pm\frac{1}{3}, \pm\frac{1}{3})$. Phenomenologically, the phase transition is described by a Landau free-energy expansion [30]

$$\mathcal{F} = \alpha(T - T_c) \sum_m |\mathbf{\Phi}_m|^2 + \beta \sum_m |\mathbf{\Phi}_m|^4 + {\sum_{m,n,k,l}}' \lambda_{mnkl} (\mathbf{\Phi}_m \cdot \mathbf{\Phi}_n)(\mathbf{\Phi}_k \cdot \mathbf{\Phi}_l) + \cdots , \quad (3)$$

where $\alpha, \beta > 0$, and the prime in the summation indicates the condition of momentum conservation, i.e., $\mathbf{q}_m + \mathbf{q}_n + \mathbf{q}_k + \mathbf{q}_l = 0$ module a reciprocal lattice vector. The overall $\mathbf{q} = (\frac{1}{3}, \frac{1}{3}, 1)$ magnetic ordering is measured by the order parameter

$$\mathcal{M} = \left(\sum_{m=1}^{12} |\mathbf{\Phi}_m|^2 \right)^{1/2} . \quad (4)$$

The temperature dependence of the $\mathcal{M}$, shown in Fig. 7(b), clearly indicates that these vector order parameters develop a nonzero expectation value at $T < T_c$, where T_c is estimated to be $0.045t$ for $J = t$. Detailed structure of this $\mathbf{q} = (\frac{1}{3}, \frac{1}{3}, 1)$ magnetic order is determined by the interaction terms λ_{mnkl}, which are very difficult to compute analytically. Our extensive Monte Carlo simulations, on the other hand, seem to observe a multitude of different magnetic structures and a possible glassy regime below T_c.

To explore this intriguing glassy phase, we compute the so-called nematic order parameter Q for spin structures obtained from our simulations. Essentially, this order parameter provides a measure of the collinearity of spins. It is given by the largest eigenvalue of the traceless matrix $\mathcal{Q}_{\mu\nu} \equiv \langle S_\mu S_\nu - \delta_{\mu\nu}/3 \rangle$ $(\mu, \nu = x, y, z)$ [31]. Interestingly, the temperature dependence of the nematic order, shown in Fig. 7(c), exhibits three branches below the critical temperature T_c, implying distinct configurations of the $\mathbf{q} = (\frac{1}{3}, \frac{1}{3}, 1)$ magnetic order. To demonstrate this quasidegeneracy directly, Fig. 8 shows the probability distribution of energy density E, magnetic order parameter $\mathcal{M}$, and spin nematic order parameter Q at three different temperatures below T_c. Interestingly, while a single prominent peak is observed in the distribution of energy and magnetic order, the histogram of the nematic order parameter Q exhibits several peaks, consistent with the multiple branches in Fig. 7(c). This finding clearly indicates a quasidegeneracy of the multiple-$\mathbf{q}$ magnetic orders, and the various quasidegenerate $\mathbf{q} = (\frac{1}{3}, \frac{1}{3}, 1)$ structures can be divided into three different groups according to their collinearity. We note that a systematic finite-size study is required in order to see whether this quasidegeneracy structure persists in the thermodynamic limit. However, due to the limitation

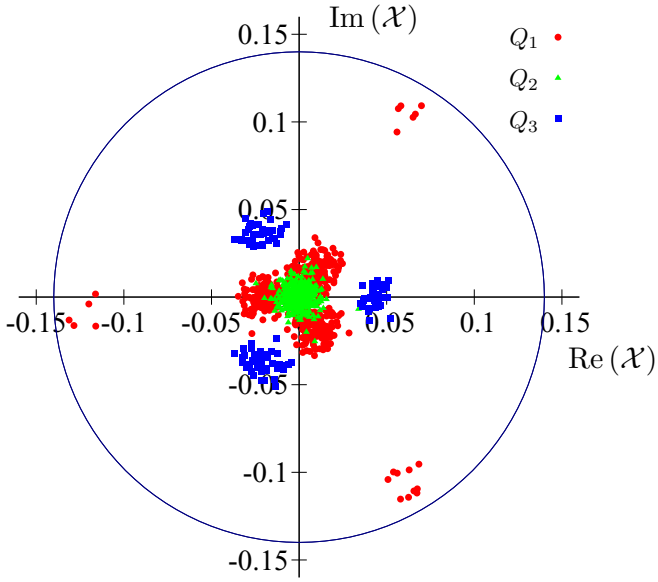

FIG. 9. Distribution for $\mathcal{X}$ in the complex plane. Red, green, and blue points represent independent samples whose nematic order parameter Q is in the left, middle, and right peaks, respectively, of the histogram $h(Q)$ in Fig. 8(b). Namely, $Q_1 \in [0, 0.17)$, $Q_2 \in [0.17, 0.23)$, $Q_3 \in [0.23, 0.3]$. The figure is obtained with 1000 samples of the system at $T = 0.03$, $J = 1$, $L = 6$.

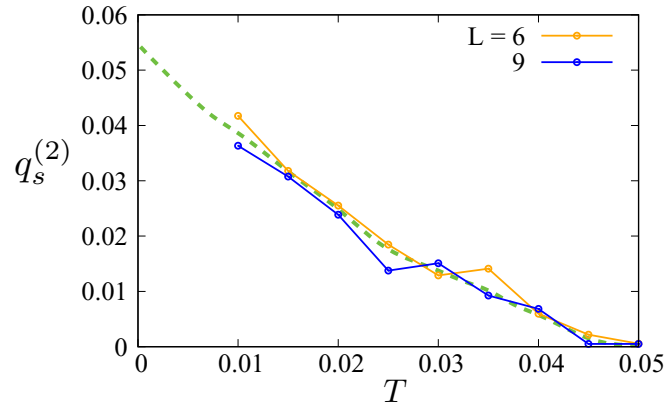

FIG. 10. The spin-freezing parameter $q_s^{(2)}$ as a function of temperature with the electron-spin coupling $J = 1$. The green dashed line is a guide to the eye. The distribution of $q_s^{(2)}$ is non-Gaussian and rather asymmetric.

of our current Monte Carlo simulations that are based on the exact diagonalization method, it is already too costly to compute the histogram for $L = 12$ lattices. Nonetheless, we have compared the histograms of $L = 6$ and 9 systems and found similar results. In fact, the multiple-peak feature is even more pronounced in the $L = 9$ histogram than in the $L = 6$ one.

Another important question is whether the cubic symmetry remains in the $\mathbf{q} = (\frac{1}{3}, \frac{1}{3}, 1)$ magnetically ordered phase. To answer this question, we first define the partial magnetic order parameters $\mathcal{M}_x$, $\mathcal{M}_y$, and $\mathcal{M}_z$, which are sum of $|\mathbf{\Phi}_m|^2$ at wave vectors $\mathbf{q}_m = (1, \pm\frac{1}{3}, \pm\frac{1}{3})$, $(\pm\frac{1}{3}, 1, \pm\frac{1}{3})$, $(\pm\frac{1}{3}, \pm\frac{1}{3}, 1)$, respectively. The dependence of these partial magnetic orders is plotted in Fig. 7(d) as function of temperature. It is apparent that the cubic symmetry in the low-T phase is conserved *in average*. However, the issue remains whether individual multi-$\mathbf{q}$ configuration preserves the cubic symmetry. To this end, we define a complex order parameter

$$\mathcal{X} = \mathcal{M}_x + \omega\mathcal{M}_y + \omega^2\mathcal{M}_z \tag{5}$$

which measures the disparity between the three partial magnetic orders; here, $\omega = e^{i\frac{2\pi}{3}}$. A symmetric phase with $\mathcal{M}_x \approx \mathcal{M}_y \approx \mathcal{M}_z$ thus gives rise to a vanishing complex order parameter $\mathcal{X} \approx 0$. Figure 9 shows the distribution of $\mathcal{X}$ obtained from 1000 independent Monte Carlo runs. Interestingly, we find strong correlation between the nematic order Q and the cubic-symmetry parameter $\mathcal{X}$. Here, magnetic orders belonging to distinct groups in the histogram (Fig. 8) are labeled by three different colors. For example, the $\mathcal{X}$ parameters corresponding to the middle peak of $h(Q)$ in Fig. 8(b) cluster around the origin, indicating that these $\mathbf{q} = (\frac{1}{3}, \frac{1}{3}, 1)$ magnetic orders approximately preserve the cubic symmetry. The two distinct parts with smaller Q illustrate the possible existence of two phases corresponding to this peak. On the other hand, magnetic orders with large Q tend to break the cubic symmetry. However, it is worth noting that the cubic symmetry is recovered when averaging over multiple domains, each characterized by a different $\mathcal{X}$ in the system. This picture of quasidegenerate multi-$\mathbf{q}$ manifold is thus consistent with the experimental observation that $GeFe_2O_4$ retains cubic symmetry in the low-T magnetic glassy phase.

We also compute the spin-freezing parameter defined as $q_{\rm SG}^{(2)} = \sum_{\mu\nu}\langle q_{\mu\nu}^2\rangle$ [32], where $q_{\mu\nu} = (1/N)\sum_i S_{i,\mu}^{(a)} S_{i,\nu}^{(b)}$ denotes the overlap of spins obtained from two replicas a and b. This parameter is nonzero when spins are frozen either in an ordered or a random configuration. Figure 10 shows the temperature dependence of the $q_{\rm SG}^{(2)}$ parameter computed from our Monte Carlo simulations for $J = 1$. The freezing parameter starts to grow at the magnetic transition point. Moreover, the curves for different lattice sizes show rather weak finite-size dependence, consistent with a first-order phase transition scenario. Extrapolating to zero temperature, we obtain a nonzero, yet rather small, $q_{\rm SG}^{(2)} \approx 0.05$. This near vanishing of the freezing parameter can be attributed to the quasidegeneracy of the multiple-$\mathbf{q}$ manifold of the $(\frac{1}{3}, \frac{1}{3}, 1)$ phase. Similar multiple-$\mathbf{q}$ glassy states have also been observed in J_1-J_2 Heisenberg pyrochlore antiferromagnets [33,34].

V. CONCLUSION AND OUTLOOK

To summarize, we have presented a thorough numerical study of a different type of itinerant frustrated magnetism on the pyrochlore lattice. In this model, the pyrochlore magnet can be viewed as a cross-linking network of Kondo chains. We have obtained the phase diagrams at two representative filling fractions $n = \frac{1}{2}$ and $\frac{2}{3}$. This model provides a natural explanation to complex spin and orbital structures observed in several spinels compound, which are very difficult to understand within localized spin models. Importantly, this magnetic phase provides a rather consistent explanation for the recently observed magnetic order in spinel $GeFe_2O_4$ [24]. In this compound, two of the six d electrons of the magnetic

Fe^{2+} ion occupy the e_g level, forming the local spins $\{\mathbf{S}_i\}$ with length $S = 1$. The other four d electrons partially fill the t_{2g} orbitals, forming quasi-1D tight-binding chains with a filling fraction $n = \frac{2}{3}$. Long-range spin order with a tripled unit cell thus naturally results from the Fermi-point nesting instability in the presence of electron-spin coupling. The resultant 3D magnetic order is then characterized by the commensurate $\mathbf{q} = (\frac{1}{3}, \frac{1}{3}, 1)$ wave vectors, which has been verified in our extensive Monte Carlo simulations.

Experimentally, neutron-scattering measurements found diffusive peaks centered at $\mathbf{q} = (\frac{1}{3}, \frac{1}{3}, 1)$ wave vectors, instead of sharp Bragg peaks. This clearly indicates a short-range spin ordering in this material. This observation can be consistent with the glassy $(\frac{1}{3}, \frac{1}{3}, 1)$ phase of our model if the correlation length of the magnetic ordering remains short in the low-temperature phase. Since the magnetic transition is first order, the correlation length remains finite throughout the phase transition. The large quasidegeneracy of spin orders in this phase also means that most likely the low-temperature phase of $GeFe_2O_4$ consists of finite domains of different magnetic structures. Since the correlation length is determined by the sizes of these domains, the diffusive peaks might result from the small magnetic domains depending on the cooling and heating procedures in the experiments.

The $\mathbf{q} = (\frac{1}{3}, \frac{1}{3}, 1)$ glassy phase is reminiscent to other magnetic glassy states reported in strongly correlated systems, including frustrated magnets [35,36], high-T_c superconducting materials [37,38], and spin-orbital Mott insulator [39]. All these states are characterized by diffuse scattering at well-defined wave vectors, indicating the short-range nature of magnetic orders. A plausible picture for these glassy magnets is the coexistence of domains with different spin structures separated by domain walls. Moreover, they also exhibit dynamical behaviors [40–42] that are different from conventional spin glass. Our work along with previous studies [33,34] suggest that multiple-$\mathbf{q}$ magnetic ordering in frustrated magnets provides a new route to realize such unconventional glassy magnets and $GeFe_2O_4$ is a potential candidate.

ACKNOWLEDGMENT

We thank X. Ke for sharing with us the unpublished experimental data and several insightful discussions. The authors also acknowledge Advanced Research Computing Services at the University of Virginia for providing technical support that has contributed to the results in this paper.

APPENDIX: 1D KONDO CHAINS

In this appendix, we consider the ground state of 1D Kondo chains, which are the backbone of the itinerant frustrated model on the pyrochlore lattice discussed in the main text. The Hamilton of a Kondo chain is

$$\mathcal{H} = -t \sum_i \sum_{\sigma=\uparrow,\downarrow} (c^\dagger_{i,\sigma} c_{i+1,\sigma} + \text{H.c.}) - J \sum_i \mathbf{S}_i \cdot \mathbf{s}_i, \quad \text{(A1)}$$

where $c^\dagger_{i,\sigma}$ is the creation operator of electrons at site i with spin σ, t is the nearest-neighbor hopping constant, J is the Hund's coupling strength, $\mathbf{S}_i$ is local magnetic moment, and $\mathbf{s}_i = \sum_{\alpha,\beta} c^\dagger_{i\alpha} \boldsymbol{\sigma}_{\alpha\beta} c_{i\beta}$ is the spin of the conduction electron. Since we are interested in magnetically ordered or glass states with frozen nonzero moments, we further assume $\mathbf{S}_i$ are classical spins with magnitude $|\mathbf{S}_i| = 1$. The zero-temperature phase diagram of the classical 1D Kondo chain in the μ-J plane, where μ is the chemical potential of the electrons, has been mapped out in Ref. [29]. Here, instead, we focus on the Kondo chain with a fixed filling fraction $n = \frac{1}{2}$ and $\frac{1}{3}$, and obtain the ground states as a function of J. Due to particle-hole symmetry, the $\frac{2}{3}$-filling case studied in the main text for the 3D pyrochlore model is equivalent to the $\frac{1}{3}$-filling case.

We perform extensive Monte Carlo simulations with Metropolis algorithm to obtain the ground states of the 1D Knodo chain. While most of the results discussed below were obtained from the chain with $N = 72$ spins, we have also conducted simulations with different chain lengths and boundary conditions (periodic vs open boundary conditions) in order to eliminate the finite-size effects. To avoid freezing problems, we started our simulations at a relatively high temperature and perform annealing simulations by slowly reducing the

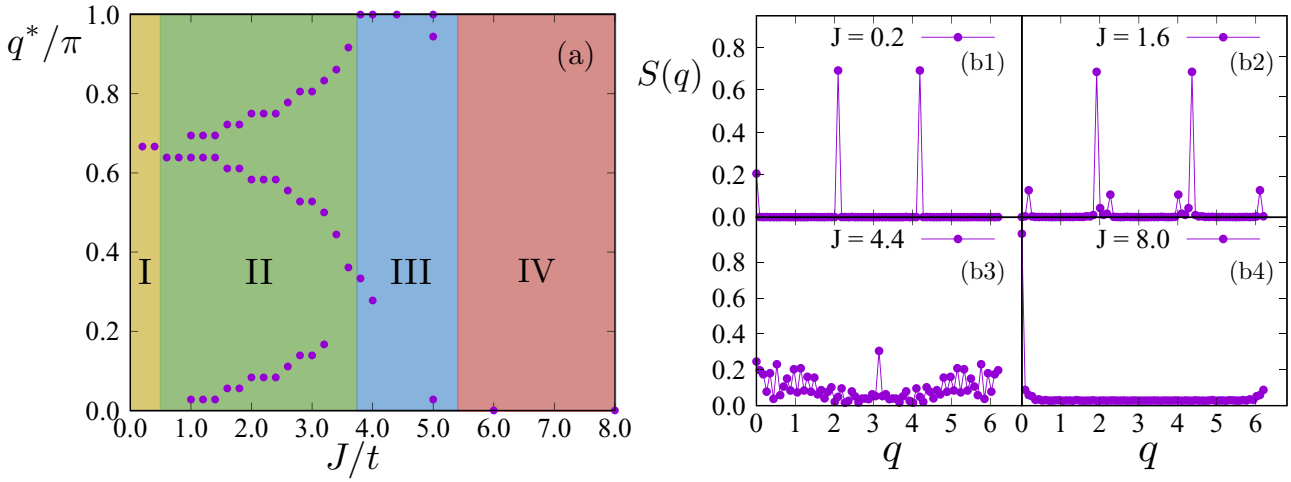

FIG. 11. (a) Wave vectors q^* where the module of $\mathbf{S}(q)$ reaches local maximum for $\frac{1}{3}$ filling. (b1)–(b4) $S(q)$ as a function of q for characteristic $J = 0.2, 1.6, 4.4, 8.0$ in regions I, II, III, IV.

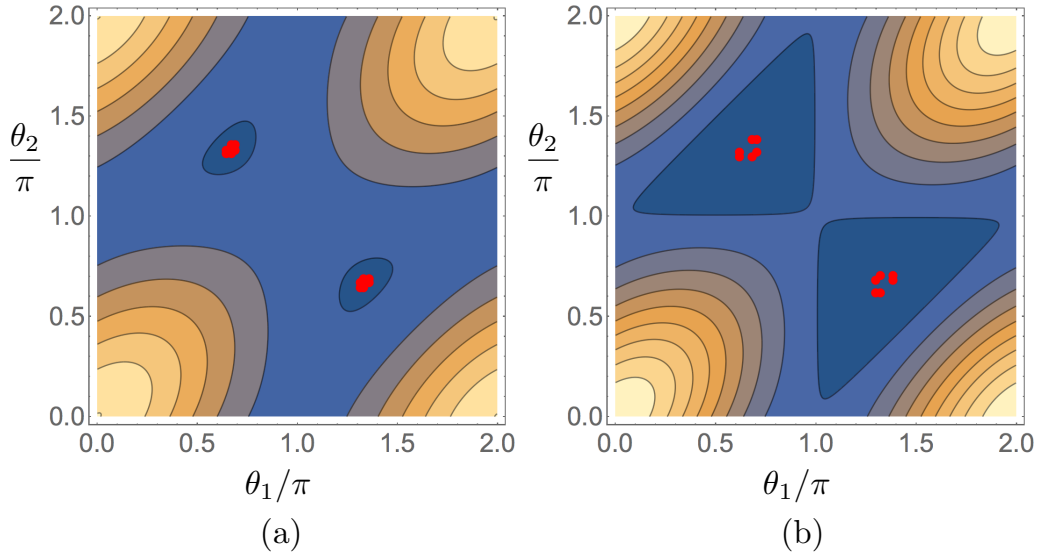

FIG. 12. Energy contour plot with respect to θ_1 and θ_2 for (a) $J = 0.2$ and (b) $J = 0.4$. The red dots indicate the optimal configuration. The range for θ_1 and θ_2 is $[0, 2\pi]$. The 12 dots represent the same or symmetry-related configuration. For $J = 0.2$, the ground state is the state such that the angles between each of the three pairs of $\mathbf{S}_0, \mathbf{S}_1, \mathbf{S}_2$ are 115.8°, 120.6°, 123.6°. For $J = 0.4$, they are 111°, 112.4°, 126.6°.

temperature. The final spin configuration is determined at $T \approx 10^{-8}$. The structure factor $S(q)$ and correlation function are evaluated and averaged at the final temperature.

We first discuss the half-filling case. Our simulations find a ground state with Néel order, i.e. $\uparrow\downarrow\uparrow\downarrow \ldots$, for all values of electron-spin coupling J, consistent with the results obtained in Ref. [29]. One can understand the stabilization of the Néel order from the weak- as well as the strong-coupling limits. In the small-J limit, the nesting of the Fermi points of a half-filled chain leads to a weak-coupling instability with respect to perturbation of Néel wave vector $q = 2k_F = \pi$. The energy of the Néel ordered state is lowered by opening a spectral gap at the Fermi points. Furthermore, our simulation finds that the energy gain is maximized by collinear Néel order. In the opposite large-J regime, the half-filled chain is a special case in the sense that there exists a macroscopic degeneracy in the $J \to \infty$ limit. In this strong-coupling limit, each site binds an electron whose spin is aligned with the local moment $\mathbf{S}_i$, whose direction can point in an arbitrary direction. As discussed in the main text, this huge degeneracy is lifted by the nearest-neighbor hopping, giving rise to an effective *antiferromagnetic* spin-spin interaction $J_{\mathrm{AF}}\mathbf{S}_i \cdot \mathbf{S}_j$, where $J_{\mathrm{AF}} \sim t^2/J > 0$. Consequently, the Néel order is also stabilized in this large-J limit. The cross-linking geometry in the pyorhclore lattice leads to geometrical frustration of Néel ordered chains. The system ends up in an all-in–all-out long-range order in which the Néel order coexists with a ferromagnetic component in each chain.

The $\frac{1}{3}$-filled Kondo chain displays a richer phase diagram as shown in Fig. 11(a). Here, we plot the wave vector q^*, which corresponds to the maxima of $S(q)$, as a function of J. At $J \lesssim 0.5$, the ground state shows a spin configuration with a period of 3, represented by a wave vector at $q^* = \frac{2}{3}\pi$, as shown in Fig. 11(b1). Again, this magnetic order arises from the weak-coupling instability due to the Fermi-point nesting $q^* = 2k_F$ for a $\frac{1}{3}$-filled chain. The wave vector $q^* = 2\pi/3$ bifurcates at $J \approx 0.5$ with one branch gradually going down and the other one rising up to $\frac{1}{2}\pi$ [see Fig. 11(b2)]. The small plateaus for q^* may result from the finite-size effects. In region III, the spin structure tends to be noncoplanar and rather complicated, represented by a less pronounced peak at $q^* = \pi$ [see Fig. 11(b3)]. Starting from $J \approx 5.5$, the ground state is ferromagnetic [Fig. 11(b4)]. The 3-period phase at small J agrees with that of 3D pyrochlore lattice, while at intermediate J, the gradual change of q^* is broken by the 3D structure and replaced by a $(\frac{1}{2}, \frac{1}{2}, \frac{1}{2})$ order. In both 1D and 3D models, a large J gives rise to the ferromagnetic phase. The evolution of the most pronounced wave vector, which is the line in the middle in region II of Fig. 11(a), shows the same trend as that of the quantum Kondo chain [28].

Here, we identify the period-3 ground state for small $J = 0.2, 0.4$ at $\frac{1}{3}$ filling. Since we expect the ground state with a 3-period structure due to the Fermi-point nesting mechanism as indicated by the Monte Carlo simulations, we can then Fourier transform the real-space Hamiltonian to a k-space Hamiltonian $\mathcal{H} = \sum_k \sum_{i,j=0}^{2} c^\dagger_{i\alpha}(k) H_{i\alpha,j\beta}(k) c_{j\beta}(k)$ in which

$$H(k) = \begin{pmatrix} -\frac{1}{2}J\boldsymbol{\sigma}\cdot\mathbf{S}_0 & -te^{ik}\sigma_0 & -te^{-ik}\sigma_0 \\ -te^{-ik}\sigma_0 & -\frac{1}{2}J\boldsymbol{\sigma}\cdot\mathbf{S}_1 & -te^{ik}\sigma_0 \\ -te^{ik}\sigma_0 & -te^{-ik}\sigma_0 & -\frac{1}{2}J\boldsymbol{\sigma}\cdot\mathbf{S}_2 \end{pmatrix}, \quad \text{(A2)}$$

where σ_0 is the 2×2 identity matrix. Working on the k space, we try to identify the lowest-energy local spin configuration. The whole spin chain is composed of multiple periodic duplicates of the first three spins $\mathbf{S}_0, \mathbf{S}_1, \mathbf{S}_2$. It is convenient to set $\mathbf{S}_0 = (0, 0, 1)$, $\mathbf{S}_1 = (\sin\theta_1, 0, \cos\theta_1)$, $\mathbf{S}_2 = (\sin\theta_2\cos\phi_2, \sin\theta_2\sin\phi_2, \cos\theta_2)$. Scanning over $\theta_1, \theta_2, \phi_2$ shows the minimum energy is obtained when $\mathbf{S}_0$, $\mathbf{S}_1$, and $\mathbf{S}_2$ are coplanar, which allows us to set $\phi_2 = 0$. We can then

scan over θ_1, θ_2 only. The final optimal configurations with $J = 0.2, 0.4$ are presented in Fig. 12. Although it is tempted to consider that the structure with the angle between any pair of spins being 120° is the best configuration, our results show that the optimal state is close to but not exactly the 120° structure and varies with J.

[1] R. Moessner and A. Ramirez, Geometrical frustration, Phys. Today **59**(2), 24 (2006).

[2] J. T. Chalker, P. C. W. Holdsworth, and E. F. Shender, Hidden Order in a Frustrated System: Properties of the Heisenberg Kagomé Antiferromagnet, Phys. Rev. Lett. **68**, 855 (1992).

[3] R. Moessner and J. T. Chalker, Properties of a Classical Spin Liquid: The Heisenberg Pyrochlore Antiferromagnet, Phys. Rev. Lett. **80**, 2929 (1998).

[4] *Introduction to Frustrated Magnetism*, edited by C. Lacroix, P. Mendels, and F. Mila, Springer Series in Solid-State Science, Vol. 164 (Springer, Berlin, 2011).

[5] L. Balents, Spin liquids in frustrated magnets, Nature (London) **464**, 199 (2010).

[6] K. I. Kugel and D. I. Khomskii, Crystal structure and magnetic properties of substances with orbital degeneracy, Zh. Eksp. Teor. Fiz. **64**, 1429 (1973) [Sov. Phys.–JETP **37**, 725 (1973)].

[7] H. Tsunetsugu and Y. Motome, Magnetic transition and orbital degrees of freedom in vanadium spinels, Phys. Rev. B **68**, 060405(R) (2003).

[8] S. Di Matteo, G. Jackeli, C. Lacroix, and N. B. Perkins, Valence-Bond Crystal in a Pyrochlore Antiferromagnet with Orbital Degeneracy, Phys. Rev. Lett. **93**, 077208 (2004).

[9] G.-W. Chern, N. B. Perkins, and Z. Hao, Quantum 120° model on pyrochlore lattice: Orbital ordering in MnV_2O_4, Phys. Rev. B **81**, 125127 (2010).

[10] P. G. Radaelli, Y. Horibe, M. J. Gutmann, H. Ishibashi, C. H. Chen, R. M. Ibberson, Y. Koyama, Y.-S. Hor, V. Kiryukhin, and S.-W. Cheong, Formation of isomorphic Ir^{3+} and Ir^{4+} octamers and spin dimerization in the spinel $CuIr_2S_4$, Nature **416**, 155 (2002).

[11] K. Takubo, S. Hirata, J.-Y. Son, J. W. Quilty, T. Mizokawa, N. Matsumoto, and S. Nagata, X-Ray Photoemission Study of $CuIr_2S_4$: Ir^{3+}-Ir^{4+} Charge Ordering and the Effect of Light Illumination, Phys. Rev. Lett. **95**, 246401 (2005).

[12] M. Schmidt, W. Ratcliff II, P. G. Radaelli, K. Refson, N. M. Harrison, and S. W. Cheong, Spin Singlet Formation in $MgTi_2O_4$: Evidence of a Helical Dimerization Pattern, Phys. Rev. Lett. **92**, 056402 (2004).

[13] S.-H. Lee, D. Louca, H. Ueda, S. Park, T. J. Sato, M. Isobe, Y. Ueda, S. Rosenkranz, P. Zschack, J. Íñiguez, Y. Qiu, and R. Osborn, Orbital and Spin Chains in ZnV_2O_4, Phys. Rev. Lett. **93**, 156407 (2004).

[14] D. I. Khomskii and T. Mizokawa, Orbitally Induced Peierls State in Spinels, Phys. Rev. Lett. **94**, 156402 (2005).

[15] G.-W. Chern and C. D. Batista, Spin Superstructure and Noncoplanar Ordering in Metallic Pyrochlore Magnets with Degenerate Orbitals, Phys. Rev. Lett. **107**, 186403 (2011).

[16] Y. Kato, Quantum Monte-Carlo study of magnetic ordering in ZnV_2O_4, Phys. Proc. **34**, 60 (2012).

[17] P. G. Radaelli, Orbital ordering in transition-metal spinels, New J. Phys. **7**, 53 (2005).

[18] V. Pardo, S. Blanco-Canosa, F. Rivadulla, D. I. Khomskii, D. Baldomir, H. Wu, and J. Rivas, Homopolar Bond Formation in ZnV_2O_4 Close to a Metal-Insulator Transition, Phys. Rev. Lett. **101**, 256403 (2008).

[19] C. Kuntscher, K. Rabia, M. K. Forthaus, M. M. Abd-Elmeguid, F. Rivadulla, Y. Kato, and C. D. Batista, Nonmonotonic evolution of the charge gap in ZnV_2O_4 under pressure, Phys. Rev. B **86**, 020405(R) (2012).

[20] M. Croft, W. Caliebe, H. Woo, T. A. Tyson, D. Sills, Y. S. Hor, S.-W. Cheong, V. Kiryukhin, and S.-J. Oh, Metal-insulator transition in $CuIr_2S_4$: XAS results on the electronic structure, Phys. Rev. B **67**, 201102 (2003).

[21] N. L. Wang, G. H. Cao, P. Zheng, G. Li, Z. Fang, T. Xiang, H. Kitazawa, and T. Matsumoto, Optical study of the metal-insulator transition in $CuIr_2S_4$ crystals, Phys. Rev. B **69**, 153104 (2004).

[22] J. Zhou, G. Li, J. L. Luo, Y. C. Ma, D. Wu, B. P. Zhu, Z. Tang, J. Shi, and N. L. Wang, Optical study of $MgTi_2O_4$: Evidence for an orbital-Peierls state, Phys. Rev. B **74**, 245102 (2006).

[23] H. X. Yang, B. P. Zhu, L. J. Zeng, H. F. Tian, C. Ma, J. Shi, and J. Q. Li, Structural modulation in the orbitally induced Peierls state of $MgTi_2O_4$, J. Phys.: Condens. Matter **20**, 275230 (2008).

[24] T. Zou, Z. Dun, T. Hong, H. Cao, C. dela Cruz, M. Gottschalk, M. Zhu, H. Zhou, and X. Ke, Spin Glass Behavior and Field Induced Anisotropic Magnetic Ordering in $S = 2$ Frustrated Spinel $GeFe_2O_4$, March Meeting Abstract K5.00009, 2016, http://meetings.aps.org/link/BAPS.2016.MAR.K5.9 (unpublished).

[25] J. C. Slater and G. F. Koster, Simplified LCAO method for the periodic potential problem, Phys. Rev. **94**, 1498 (1954).

[26] J. Kanamori, Electron correlation and ferromagnetism of transition metals, Prog. Theor. Phys. **30**, 275 (1963).

[27] H. Tsunetsugu, M. Sigrist, and K. Ueda, The ground-state phase diagram of the one-dimensional Kondo lattice model, Rev. Mod. Phys. **69**, 809 (1997).

[28] D. J. Garcia, K. Hallberg, B. Alascio, and M. Avignon, Spin Order in One-Dimensional Kondo and Hund Lattices, Phys. Rev. Lett. **93**, 177204 (2004).

[29] S. Minami and H. Kawamura, Low-temperature magnetic properties of the kondo lattice model in one dimension, J. Phys. Soc. Jpn. **84**, 044702 (2015).

[30] J. N. Reimers, A. J. Berlinsky, and A.-C. Shi, Mean-field approach to magnetic ordering in highly frustrated pyrochlores, Phys. Rev. B **43**, 865 (1991).

[31] P. M. Chaikin and T. C. Lubensky, *Principles of Condensed Matter physics* (Cambridge University Press, Cambridge, 1995).

[32] D. X. Viet and H. Kawamura, Numerical Evidence of Spin-Chirality Decoupling in the Three-Dimensional Heisenberg Spin Glass Model, Phys. Rev. Lett. **102**, 027202 (2009).

[33] G.-W. Chern, R. Moessner, and O. Tchernyshyov, Partial order from disorder in a classical pyrochlore antiferromagnet, Phys. Rev. B **78**, 144418 (2008).

[34] T. Okubo, T. H. Nguyen, and H. Kawamura, Cubic and noncubic multiple-q states in the Heisenberg antiferromagnet on the pyrochlore lattice, Phys. Rev. B **84**, 144432 (2011).

[35] M. J. P. Gingras, C. V. Stager, N. P. Raju, B. D. Gaulin, and J. E. Greedan, Static Critical Behavior of the Spin-Freezing Transition in the Geometrically Frustrated Pyrochlore Antiferromagnet $Y_2Mo_2O_7$, Phys. Rev. Lett. **78**, 947 (1997).

[36] A. Samarakoon, T. J. Sato, T. Chen, G.-W. Chern, J. Yang, I. Klich, R. Sinclair, H. Zhou, and S.-H. Lee, Aging, memory, and nonhierarchical energy landscape of spin jam, Proc. Natl. Acad. Sci. USA **113**, 11806 (2016).

[37] M. Matsuda, M. Fujita, K. Yamada, R. J. Birgeneau, M. A. Kastner, H. Hiraka, Y. Endoh, S. Wakimoto, and G. Shirane, Static and dynamic spin correlations in the spin-glass phase of slightly doped $La_{2-x}Sr_xCuO_4$, Phys. Rev. B **62**, 9148 (2000).

[38] N. Katayama, S. Ji, D. Louca, S.-H. Lee, M. Fujita, T. J. Sato, J. Wen, Z. Xu, G. Gu, G. Xu, Z. Lin, M. Enoki, S. Chang, K. Yamada, and J. M. Tranquada, Investigation of the spin-glass regime between the antiferromagnetic and superconducting phases in $Fe_{1+y}Se_xTe_{1-x}$, J. Phys. Soc. Jpn. **79**, 113702 (2010).

[39] Y. Luo, C. Cao, B. Si, Y. Li, J. Bao, H. Guo, X. Yang, C. Shen, C. Feng, J. Dai, G. Cao, and Z.-A. Xu, Li_2RhO_3: A spin-glassy relativistic Mott insulator, Phys. Rev. B **87**, 161121(R) (2013).

[40] B. I. Halperin and W. M. Saslow, Hydrodynamic theory of spin waves in spin glasses and other systems with noncollinear spin orientations, Phys. Rev. B **16**, 2154 (1977).

[41] D. F. Mross and T. Senthil, Spin- and Pair-Density-Wave Glasses, Phys. Rev. X **5**, 031008 (2015).

[42] A. M. Samarakoon, M. Takahashi, D. Zhang, J. Yang, N. Katayama, R. Sinclair, H. D. Zhou, S. O. Diallo, G. Ehlers, D. A. Tennant, S. Wakimoto, K. Yamada, G.-W. Chern, T. J. Sato, S.-H. Lee, Scaling of memories and crossover in glassy magnets, Sci. Rep. **7**, 12053 (2017).